Deviation from bulk in the pressure-temperature phase diagram of V$_2$O$_3$ thin films

I. Valmianski,[1] Juan Gabriel Ramirez,[2] C. Urban,[1] X. Batlle,[3] and Ivan K. Schuller[1]

[1]*Center for Advanced Nanoscience, Physics Department, University of California, San Diego, California 92093, USA*

[2]*Department of Physics, Universidad de los Andes, Bogotá 111711, Colombia*

[3]*Departament de Física de la Matèria Condensada and Institut de Nanociència i Nanotecnologia,*
Universitat de Barcelona, 08028 Barcelona, Catalonia, Spain

We found atypical pressure dependence in the transport measurements of the metal to insulator transition (MIT) in epitaxial thin films of vanadium sesquioxide (V$_2$O$_3$). Three different crystallographic orientations and four thicknesses, ranging from 40 to 500 nm, were examined under hydrostatic pressures (P$_h$) of up to 1.5 GPa. All of the films at transition exhibited a four order of magnitude resistance change, with transition temperatures ranging from 140 to 165 K, depending on the orientation. This allowed us to build pressure-temperature phase diagrams of several orientations and film thicknesses. Interestingly, for pressures below 500 MPa, all samples deviate from bulk behavior and show a weak transition temperature (T_c) pressure dependence ($dT_c/dP_h = 1.2 \times 10^{-2} \pm 0.3 \times 10^{-2}$ K/MPa), which recovers to bulklike behavior ($3.9 \times 10^{-2} \pm 0.3 \times 10^{-2}$ K/MPa) at higher pressures. Furthermore, we found that pressurization leads to morphological but not structural changes in the films. This indicates that the difference in the thin film and bulk pressure-temperature phase diagrams is most probably due to pressure-induced grain boundary relaxation, as well as both plastic and elastic deformations in the film microstructure. These results highlight the difference between bulk and thin films behaviors.

I. INTRODUCTION

The metal to insulator transition (MIT) in vanadium sesquioxide has been a topic of intense study; V$_2$O$_3$ has an unusual MIT because it coincides with a structural phase transition (SPT) and a magnetic phase transition (MPT) [1,2]. The co-occurrence of multiple phase transitions raises not only interesting questions about the underlying driving mechanisms but also presents new opportunities for device applications, such as infrared imaging, spintronic devices, resistive switching devices, field-effect transistors, and magnetoelastically coupled recording media [3–8].

The MIT in V$_2$O$_3$ has been studied in a vacuum as a function of temperature and applied voltage both in bulk and in thin films [2,9–12]. Furthermore, the pressure dependence of MIT has been studied in bulk in the (V$_{1-x}$Cr$_x$)$_2$O$_3$ system [13–15]. In this system, the MIT can be induced by decreasing the temperature (at sufficiently small Cr concentration), by decreasing x or by increasing the pressure P. Studies have suggested that doping with Cr is equivalent to an applied pressure ($x = 0.01$ corresponds to 4 kbar). The occurrence of the MIT and the SPT with a complex phase diagram suggests a coupling between electronic and lattice degrees of freedom. The question whether this coupling remains when the material is clamped to a substrate is of fundamental importance. For instance, in some materials, the pressure dependence deviates from its bulk behavior. This is mainly due to (i) geometric anisotropy that arises when grain size is commensurate with the film thickness, making the film quasi-two dimensional, (ii) substrate clamping that affects thin films under pressure by fixing their in-plane elastic response [16], or (iii) complex thin film microstructure that can affect many properties by changing local strain [17–19]. All the above properties can be distinguished by studying the film response with pressure, varying either the film thickness or the film orientation. A detailed analysis of the pressure dependence of the MIT in

V$_2$O$_3$ thin films was lacking in the literature, before the present studies.

In this paper, we present temperature-dependent transport measurements of V$_2$O$_3$ thin films under pressure as a function of both film thickness and crystallographic orientation in the low positive pressure regime (vacuum to 1.5 GPa) and compare them to bulk measurements. We examine three different crystallographic orientations to investigate substrate clamping effects and four different thicknesses to research geometric anisotropy and out-of-plane relaxation. Structural and morphological measurements before and after pressurization provide information on the microstructural changes due to pressurization.

II. EXPERIMENTAL

The V$_2$O$_3$ thin films were prepared in a high-vacuum sputter deposition system with base pressure of 1×10^{-7} Torr. All samples were grown on Al$_2$O$_3$ substrates. Four different film thicknesses, 40, 60, 100, and 500 nm, were prepared on (0 1 2) r-plane orientation of Al$_2$O$_3$. Furthermore, 100 nm V$_2$O$_3$ films were also grown on (1 0 0) m-plane and (1 1 0) a-plane Al$_2$O$_3$ orientations. All growth was performed at 750 °C in 4 mTorr of ultrahigh purity (UHP) Ar by rf magnetron sputtering at 100 W of a V$_2$O$_3$ target. The x-ray characterization, including x-ray reflectivity (XRR) for thickness measurements, as well as x-ray diffraction (XRD) and reciprocal space mapping (RSM) for structural measurements, was carried out using a Rigaku SmartLab x-ray diffractometer. Fitting to the XRR data was done using MotoFit complex scattering length density (SLD) fitting functionality [20]. The morphology of the thin films at room temperature was investigated with a Veeco scanning probe microscope operating in a tapping mode as an atomic force microscope (AFM).
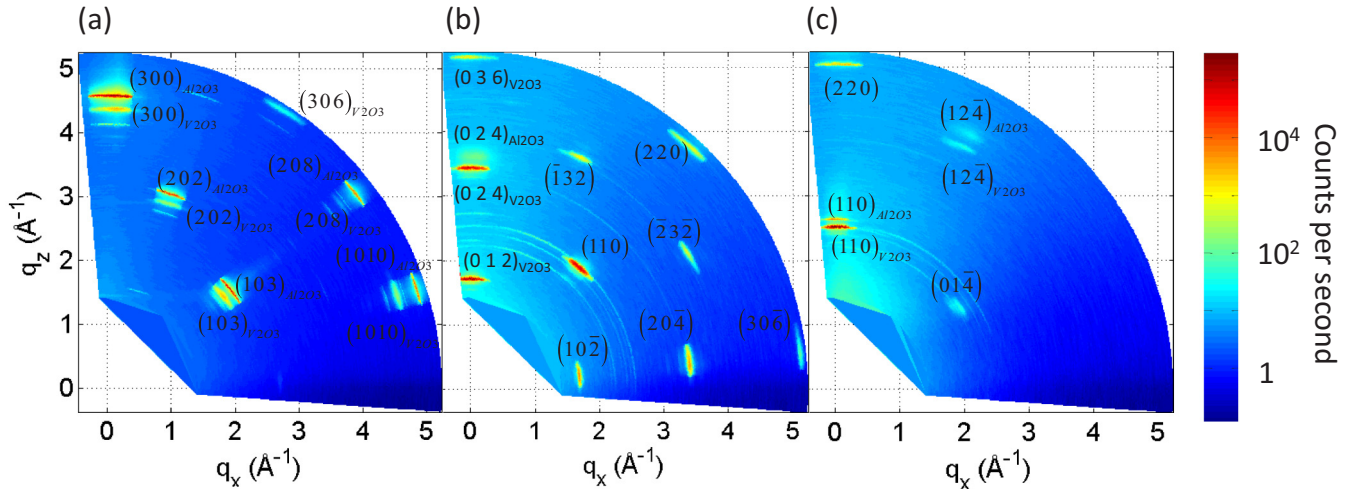
FIG. 1. The RSM for V_2O_3 100 nm films grown on different orientations of Al_2O_3. The data at $q_x = 0$ represents the typical out-of-plane measurement. The RSM for film grown on (a) a-plane (1 0 0) out-of-plane orientation. Both V_2O_3 and Al_2O_3 peaks are visible. Both in-plane and out-of-plane crystallographic orientations in V_2O_3 follow the Al_2O_3 orientations. Films grown on (b) r-plane (0 1 2; sapphire peaks are not visible due to a slight miscut in the substrate) and (c) m-plane (1 1 0). For the (2 2 0) plane, only the V_2O_3 peak is visible because the Al_2O_3 peak is outside the scan range. In (b) and (c), faint polycrystalline rings (two to three orders of magnitude more faint than the associated peaks) are visible, suggesting that a small portion of the film is polycrystalline. The measurements were done without a monochromator to increase the overall diffraction intensity, which resulted in the presence of several contamination lines. The primary x-ray wavelength is 1.5406 Å associated with Cu $K\alpha 1$; however, significant contributions to the detected signal come from Cu $K\alpha 2$ ($\lambda = 1.5444$ Å) and W L1 ($\lambda = 1.0248$ Å). For example, in Fig. 3(a), the (300) peak has another peak below the (300)V_2O_3 associated with the W L1 of (300)Al_2O_3 and an even more faint fourth peak from W L1 of (300)V_2O_3.

Pressurization was performed at room temperature from atmospheric pressure to 1.5 GPa in a hydrostatic pressure cell Pcell 30 from Almax EasyLab using a 5 ton press. Pentane was used as the pressure medium, which does not chemically interact with V_2O_3. Pressure was calculated using the resistance of a manganese manometer placed inside the cell, before and after the temperature scan. Resistance of the V_2O_3 film was concurrently measured during pressurization. Both resistance measurements were performed in a pseudo-four-probe configuration with a Keithley 6221A ac current source and Keithley 2181A nanovoltmeter. The applied pressure as measured by the press manometer was also recorded. This showed the expected linear relationship with the pressure as measured by the manganese manometer inside the cell.

The MIT measurements were performed by placing the pressurized Pcell 3000 into a Quantum Design Physical Property Measurement System (PPMS)-DynaCool with electrical contacts connected to an external Keithley 6221A ac current source and Keithley 2181A nanovoltmeter similar to the ones used during pressurization. A 100 nA constant current was applied, and the voltage drop was measured. The low current was needed to accommodate the very large resistance change in the sample. The electrical transport measurement setup and the cryostat were controlled using a custom routine in the National Instruments LabVIEW software. The pressure cell was initially cooled at 10 K/min to a starting temperature well above the transition and then allowed to stabilize for 1 h. To measure the cooling branch of the MIT, the temperature was decreased at a rate of 0.1 K/min to a final temperature below the MIT. Finally, the temperature was raised at 0.1 K/min to the starting temperature to measure the heating branch of the MIT. A slow temperature scan rate was used to minimize the

internal thermal lag inside the pressure cell, while measuring both decreasing and increasing temperature branches of the MIT. Once the full MIT hysteresis was measured, the pressure cell was heated to 300 K and left for 1 h to stabilize. It was then removed from the cryostat and further pressurized to the next pressure value after which the resistance measurement process was repeated. Because of possible pressure media leaks, the pressure cell could not be depressurized to a controlled pressure (above atmosphere).

III. RESULTS AND DISCUSSION

Results of x-ray RSM of 100 nm V_2O_3 films grown on r-plane (0 1 2), m-plane (1 0 0), and a-plane (1 1 0) orientations of Al_2O_3 are shown in Fig. 1. All of the films follow the in-plane and out-of-plane crystallographic directions of the substrate and are thus epitaxial. This means that we can control which crystallographic orientation of V_2O_3 is unclamped when pressurized. The V_2O_3 lattice constants are identical to bulk values, within the resolution of the measurement system. This is surprising since there is a lattice mismatch ($a_{Al_2O_3} = 4.785$ Å, $a_{V_2O_3} = 4.9492$ Å, $c_{Al_2O_3} = 12.991$ Å, $c_{V_2O_3} = 13.9980$ Å). A possible explanation is the presence of an intermediate interfacial layer, as previously reported for VO_2 and other oxide heterostructures [21] or a weak overlayer-substrate interaction, as present in many lattice mismatched epitaxial systems [22]. Note that the elastic moduli for bulk V_2O_3 and Al_2O_3 are 400 and 450 GPa, respectively, with weak directional dependence. Furthermore, thin films tend to have larger elastic moduli than bulk, which means the V_2O_3 can be even harder.
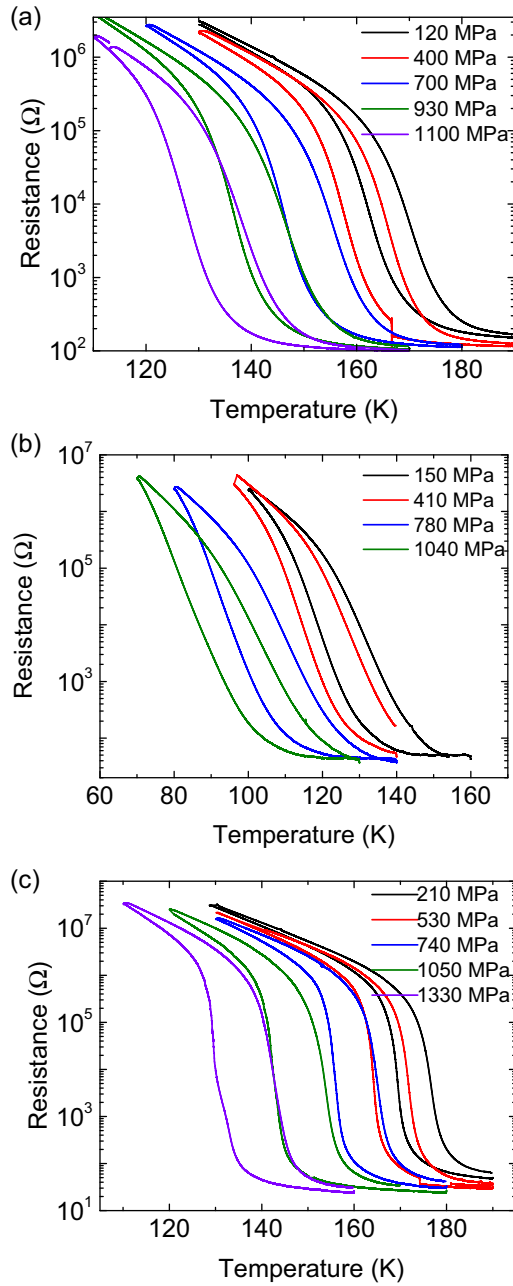
FIG. 2. Resistance versus temperature dependence at different pressures for (a) *r* plane, (b) *a* plane, and (c) *m* plane. The transition temperature decreases monotonically with increased pressure. Only absolute resistance measurements are reported because the samples were small <1 mm^2) and the variation in the geometry of the indium contact point made accurate evaluation of resistivity across the sample difficult. However, the magnitude and shape of transition is comparable or better to those previously reported in literature (larger change, sharper transition) [18,23]. The difference in shape of the curves can be attributed to interfacial microstructure [18,24].

The pressure and temperature dependences of the resistance of the thin films grown on the three different orientations are shown in Fig. 2. All of the films present a MIT with roughly four orders of magnitude resistance change and display a thermal hysteresis between the cooling and warming branches of about 10 K. The transition temperature of the MIT is defined
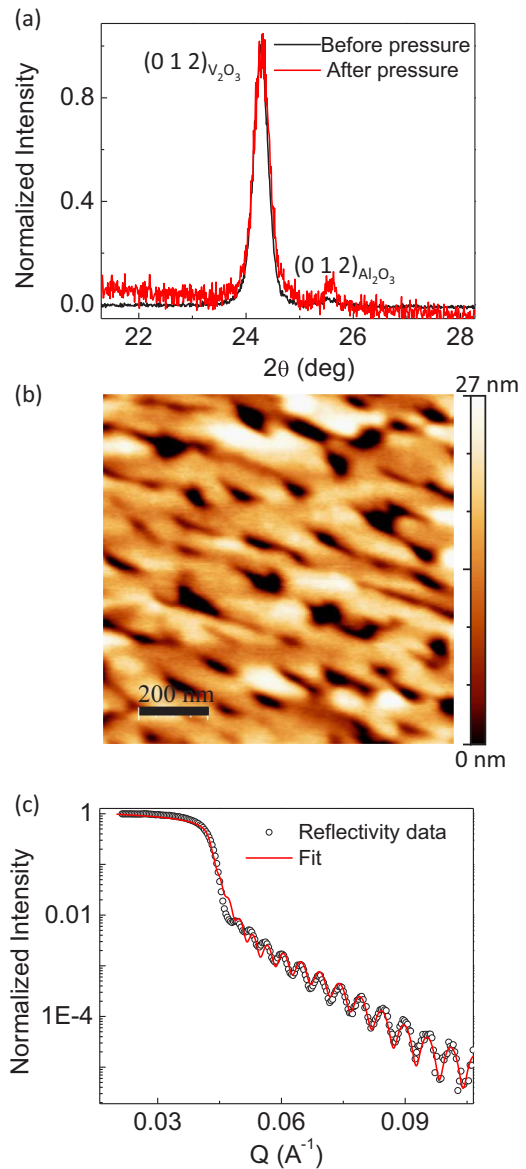

FIG. 3. Structural and microstructural characterization of a 100 nm V$_2$O$_3$ thin film grown on *r*-plane Al$_2$O$_3$: (a) XRD of the (0 1 2) out-of-plane peak before and after pressurization. Since the pressure cell accepts only very small sample sizes (less than 1 × 1 mm^2), the pattern after pressurization is noisier. (b) AFM image after pressurization; (c) XRR data and fit of data, before pressurization ($\chi^2 = 0.0198$). Reflectivity data after pressurization not shown since very noisy.

as the inflection point in the logarithm of the resistance of the cooling branch. We chose the cooling branch to avoid a possibility of minor loops in the hysteresis. All of the measurements start with the sample at room temperature (at which pressurization occurs), where the material is in the metallic state. Then, the film is monotonically cooled into the insulating state, and, after reaching the minimum temperature, it is warmed back to room temperature. Once at room temperature, the pressure in the pressure cell is increased, and the temperature scan is repeated.
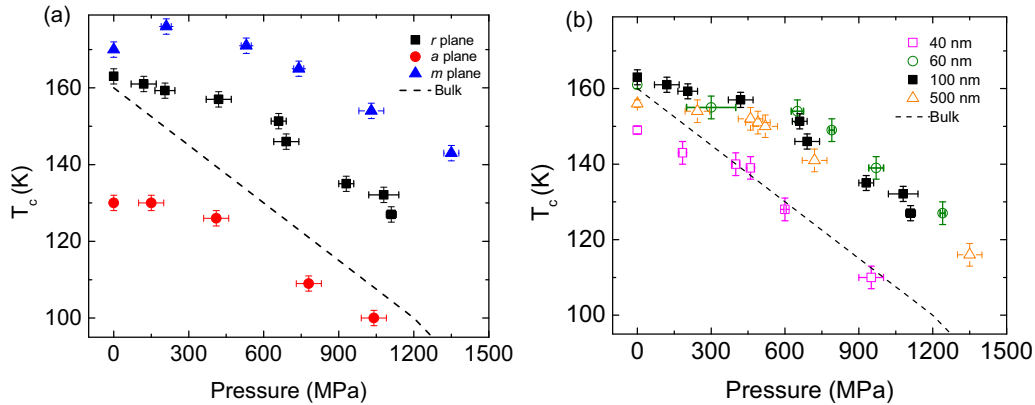
FIG. 4. Transition temperature as a function of pressure. In both panels, the dashed line represents the experimental single crystal bulk behavior [28]. (a) Phase diagrams plotted as a function of crystallographic orientation for 100 nm thin films. (b) Phase diagrams plotted as a function of film thickness for r-cut sapphire. The uncertainty in pressure was determined from a pressure measurement before and after the temperature sweep. The 3 K uncertainty in transition temperature is a worst case uncertainty in the location of the inflection point in the curve.

The cooling and heating branches do not close at low temperature because of the persistence of microinclusions of metallic domains in the insulating phase even after most of the transition has occurred. This has been previously observed using first order reversal curve (FORC) measurements in VO_2 [25]. The substrate dependence of the transition temperature and hysteresis loop shape has also been observed under vacuum measurements and was attributed to two factors [18,23]. First, various Al_2O_3 substrate orientations substrates have different surface terracing. The resulting morphology generates strain in the V_2O_3 grains, which can be modified by annealing the substrate before growth. Second, various substrate orientations have different lattice mismatches. These two factors are also the reason why it is very difficult to grow V_2O_3 with several orders of magnitude MIT on c-plane (1 0 0) Al_2O_3 [18].

The XRD patterns and AFM images before and after the pressurization are shown in Fig. 3. Figure 3(a) shows the (0 1 2) Bragg peak of a 100 nm V_2O_3 grown on the r-plane Al_2O_3 before and after pressurization. There is no change in the peak position, which suggests that there are no structural changes. Figure 3(b) shows an AFM image of the same film. Analysis of the latter for pressure effects on the microstructure reveals changes in roughness. For example, for this particular sample, three areas, several millimeters apart, were measured before and after pressurization. The root-mean-square roughness changes from 7.5 nm before to 6.1 nm after pressurization (p-value < 0.001). This suggests that while pressurization does not induce atomic scale structural changes, it does cause microstructural changes. Furthermore, the numerous morphological indentations seen in the AFM image can yield additional mechanisms for strain relaxation. Figure 3(c) shows XRR with a fit for nominally 100-nm-thick V_2O_3 film grown on the r-plane Al_2O_3. The fit is performed by using a two-layer model with a 100 nm bottom layer (1 nm roughness) and an 8 nm top layer (3.3 nm roughness), with lower density on top of a 1.2 nm rough substrate. The top layer is likely oxygen oversaturated due to exposure to air. The differences between the fit and the data in the low Q range are probably due to the top layer having a nonuniform electron scattering length density

(eSLD). The real part of the eSLD is linearly proportional to the material density. The fitted real part of the eSLD of the bottom layer of the 100 nm film is $(36.2 \pm 0.2) \cdot 10^{-6}/\text{Å}^2$, as compared to the nominal value of $38.8 \times 10^{-6}/\text{Å}^2$, for the bulk counterpart. Literature values of the imaginary component of the eSLD were used [26]. This strongly implies that the V_2O_3 thin film has a density 6.6% lower than the bulk material.

The pressure-temperature phase diagrams extracted from the transport measurements in Fig. 3 are displayed in Fig. 4. Figure 4(a) shows that different crystal orientations have different transition temperatures. The m-plane and r-plane oriented films have transition temperatures consistently above that of the bulk material, while the a-plane oriented film has a transition temperature below the bulk material. Figure 4(b) shows the phase diagram for different thicknesses: 40-, 60-, 100-, and 500-nm-thick films grown on r-plane sapphire. The 40 nm film shows a transition temperature shifted to lower temperatures, because the film thickness is lower than the lateral grain size, which possibly affects the long-range order responsible for the MIT. Furthermore, at lower thicknesses, interfacial effects become more predominant. The 100- and 500-nm-thick films show nearly identical behavior since their thickness is larger than the lateral grain size. At room temperature, the boundaries expected are only low-angle grain boundaries [27]. At low temperature, below the MIT, additional boundaries appear due to crystal twining.

The most striking result appears when a constant T offset is subtracted from each of the curves in Fig. 4. The new pressure dependences are shown in Fig. 5: the pressure dependence of all samples grown on different orientation substrates and with different thicknesses collapse onto two single master lines that significantly deviate from the bulk behavior. Thin films present two pressure dependence regimes. Below 500 MPa, a weaker pressure dependence than in bulk is observed, with a critical temperature-pressure slope of 1.2×10^{-2} K/MPa. This region is referred to as the *small slope regime*. In contrast, above 500 MPa, the pressure dependence is similar to the bulk behavior with a temperature-pressure slope of 3.9×10^{-2} K/MPa,
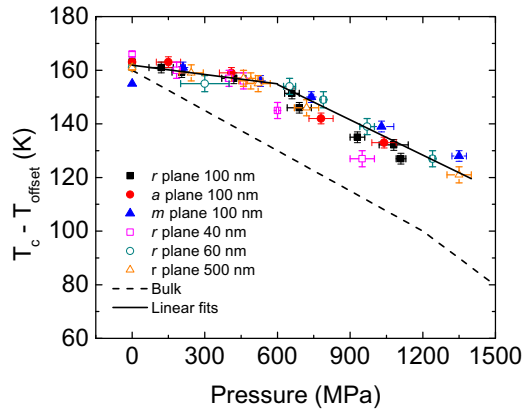
FIG. 5. Transition temperature as a function of pressure, with a constant T offset subtracted from each of the phase diagrams in Fig. 4. All data collapse onto two master lines (below 600 MPa, slope -0.012 ± 0.003 K/MPa and above 600 MPa, -0.039 ± 0.003 K/MPa); a *small slope region* and a *large slope region*. Dashed line represents the experimental single crystal bulk behavior with a slope of 0.05 K/MPa [28].

IV. CONCLUSIONS

Pressure-dependent measurements help understanding the nature of the MIT and the SPT in V_2O_3. The thin film dependence of V_2O_3 in the application-relevant low positive pressure regime between 0 and 1.5 GPa is reported. We have found that a transition temperature of V_2O_3 thin films show two pressure dependencies: smaller than in bulk below 500 MPa and similar to bulk, above 500 MPa. This feature is unique to all thin films measured in this paper and has not been observed in the bulk counterpart. Furthermore, the effect is largely independent of film orientation or thickness, which is likely because the films are not fully compact (thin film density is 6.6% lower than bulk value) and undergo strain relaxation when pressurized. This strain relaxation occurs both in grain boundaries and in morphological defects in the film. When the stress relaxation mechanisms become exhausted, the behavior of the film becomes the same as in bulk. These findings are further supported because there are no structural changes in the films before and after pressurization, while there is a slight change in the film microstructure. This is especially relevant for developing SPT-based heterostructure devices since they often operate through elastic coupling with the V_2O_3 layer.

which we refer to as the *large slope regime*. Moreover, the difference between large and small slope regimes is much more pronounced than the variation of the V_2O_3 thin film behavior with either crystallographic orientation or thickness, which suggests that they are physically relevant.

We propose that the two-slope regime is due to the effective porosity of the films. As observed in the AFM images [Fig. 3(b)] and XRR data [Fig. 3(c)], the films are not uniformly dense, which allows for reversible grain boundary relaxation when pressurized. As the films are epitaxial (Fig. 1), they are clamped to the substrate and relax back to the porous state when the pressure is removed. The small morphological changes seen in the AFM images are due to small plastic deformations in the relaxation process.

This mechanism has been extensively studied for foam materials, which also exhibit a kink in their stress-strain dependence, showing a low stress dependence at low pressure and bulklike behavior at high pressure [29–31]. In fact, qualitatively the change in slope in Fig. 5 is consistent with a simple model that assumes the pressure to be isotropic in the substrate and the film to be experiencing a reduced in-plane pressure due to strain relaxation within boundaries. Then, with increasing pressure, the relaxation mechanism becomes exhausted and the film behaves bulklike (see Supplemental Material [32]).

This paper is the result of highly collaborative research. The experiments were conceived jointly, the data were extensively debated, and the paper underwent multiple iterations among all the coauthors. Samples were fabricated, characterized, and measured at the University California, San Diego.

[1] M. Imada, A. Fujimori, and Y. Tokura, Rev. Mod. Phys. **70**, 1039 (1998).

[2] B. Sass, C. Tusche, W. Felsch, N. Quaas, A. Weismann, and M. Wenderoth, J. Phys.: Condens. Matter **16**, 77 (2004).

[3] D. Ruzmetov, G. Gopalakrishnan, C. Ko, V. Narayanamurti, and S. Ramanathan, J. Appl. Phys. **107**, 114516 (2010).

[4] Z. Yang, C. Ko, and S. Ramanathan, Annu. Rev. Mater. Res. **41**, 337 (2011).

[5] A. Sharoni, J. G. Ramírez, and I. K. Schuller, Phys. Rev. Lett. **101**, 026404 (2008).

[6] B. Sass, C. Tusche, W. Felsch, F. Bertran, F. Fortuna, P. Ohresser, and G. Krill, Phys. Rev. B **71**, 014415 (2005).

[7] S. Lupi, L. Baldassarre, B. Mansart, A. Perucchi, A. Barinov, P. Dudin, E. Papalazarou, F. Rodolakis, J.-P. Rueff, J.-P. Itié, S. Ravy, D. Nicoletti, P. Postorino, P. Hansmann, N. Parragh, A. Toschi, T. Saha-Dasgupta, O. K. Andersen, G. Sangiovanni, K. Held, *et al.* Nat. Commun. **1**, 105 (2010).

[8] T. Saerbeck, J. de la Venta, S. Wang, J. G. Ramírez, M. Erekhinsky, I. Valmianski, and I. K. Schuller, J. Mater. Res. **29**, 2353 (2014).

[9] A. Zimmers, L. Aigouy, M. Mortier, A. Sharoni, S. Wang, K. G. West, J. G. Ramirez, and I. K. Schuller, Phys. Rev. Lett. **110**, 056601 (2013).

[10] S. Guénon, S. Scharinger, S. Wang, J. G. Ramírez, D. Koelle, R. Kleiner, and I. K. Schuller, EPL **101**, 57003 (2013).

[11] J. Brockman, N. P. Aetukuri, T. Topuria, M. G. Samant, K. P. Roche, and S. S. P. Parkin, Appl. Phys. Lett. **98**, 152105 (2011).

[12] J. Jeong, N. Aetukuri, T. Graf, T. D. Schladt, M. G. Samant, and S. S. P. Parkin, Science **339**, 1402 (2013).

[13] D. B. McWhan, J. P. Remeika, T. M. Rice, W. F. Brinkman, J. P. Maita, and A. Menth, Phys. Rev. Lett. **27**, 941 (1971).

[14] S. A. Carter, T. F. Rosenbaum, M. Lu, H. M. Jaeger, P. Metcalf, J. M. Honig, and J. Spalek, Phys. Rev. B **49**, 7898 (1994).

[15] H. Kuwamoto, J. M. Honig, and J. Appel, Phys. Rev. B **22**, 2626 (1980).

[16] S. L. Bud'ko, J. Guimpel, O. Nakamura, M. B. Maple, and I. K. Schuller, Phys. Rev. B **46**, 1257 (1992).

[17] H. W. Jang, A. Kumar, S. Denev, M. D. Biegalski, P. Maksymovych, C. W. Bark, C. T. Nelson, C. M. Folkman, S. H. Baek, N. Balke, C. M. Brooks, D. A. Tenne, D. G. Schlom, L. Q. Chen, X. Q. Pan, S. V. Kalinin, V. Gopalan, and C. B. Eom, Phys. Rev. Lett. **104**, 197601 (2010).

[18] J. Brockman, M. G. Samant, K. P. Roche, and S. S. P. Parkin, Appl. Phys. Lett. **101**, 051606 (2012).

[19] A. T. Wong, C. Beekman, H. Guo, W. Siemons, Z. Gai, E. Arenholz, Y. Takamura, and T. Z. Ward, Appl. Phys. Lett. **105**, 052401 (2014).

[20] A. Nelson, J. Appl. Crystallogr. **39**, 273 (2006).

[21] S. J. Pennycook, H. Zhou, M. F. Chisholm, A. Y. Borisevich, M. Varela, J. Gazquez, T. J. Pennycook, and J. Narayan, Acta Mater. **61**, 2725 (2013).

[22] L. Dong, J. Schnitker, R. W. Smith, and D. J. Srolovitz, J. Appl. Phys. **83**, 217 (1998).

[23] B. S. Allimi, S. P. Alpay, C. K. Xie, B. O. Wells, J. I. Budnick, and D. M. Pease, Appl. Phys. Lett. **92**, 202105 (2008).

[24] H. Schuler, S. Klimm, G. Weissmann, C. Renner, and S. Horn, Thin Solid Films **299**, 119 (1997).

[25] J. G. Ramírez, A. Sharoni, Y. Dubi, M. E. Gómez, and I. K. Schuller, Phys. Rev. B **79**, 235110 (2009).

[26] V. F. Sears, Neutron News **3**, 26 (1992).

[27] J. De La Venta, S. Wang, T. Saerbeck, J. G. Ramírez, I. Valmianski, and I. K. Schuller, Appl. Phys. Lett. **104**, 062410 (2014).

[28] A. Jayaraman, D. B. McWhan, J. P. Remeika, and P. D. Dernier, Phys. Rev. B **2**, 3751 (1970).

[29] F. Triawan, K. Kishimoto, T. Adachi, K. Inaba, T. Nakamura, and T. Hashimura, Acta Mater. **60**, 3084 (2012).

[30] O. E. Petel, S. Ouellet, A. J. Higgins, and D. L. Frost, Shock Waves **23**, 55 (2013).

[31] K. Y. G. McCullough, N. A. Fleck, and M. F. Ashby, Acta Mater. **47**, 2323 (1999).

[32] See Supplemental Material at http://link.aps.org/supplemental/10.1103/PhysRevB.95.155132 for the description of strain relaxation analytical model.